Journal of the Meteorological Society of Japan

EARLY ONLINE RELEASE

The DOI for this manuscript is
DOI:10.2151/jmsj.2024-008
J-STAGE Advance published date: December 28, 2023
The final manuscript after publication will replace the preliminary version at the above DOI once it is available.

JMSJ-2023-0015.R4

Windward Region Sensitivity and its Effects on Heavy Rainfall Prediction Investigated with Ensemble Systems

Daichi TOYOOKA

Graduate School of Life and Environmental Sciences,

University of Tsukuba, Tsukuba, Japan

Takuya KAWABATA

Meteorological Research Institute,

Japan Meteorological Agency, Tsukuba, Japan

and

H. L. TANAKA

Center for Computational Sciences, University of Tsukuba

20 November, 2023

----

1) Corresponding author: Takuya Kawabata, Meteorological Research Institute, Japan Meteorological Agency, 1-1 Nagamine, Tsukuba, Ibaraki, Japan

E-mail: tkawabat@mri-jma.go.jp

Abstract

In this study, we investigated how the prediction on the record-breaking heavy rainfall event that occurred in western Japan in July 2018 was affected by the initial conditions. The most sensitive region was identified and its impact on the verification region was described through ensemble forecasting. Backward trajectory and ensemble sensitivity analyses were conducted to determine the origin of the air mass that reached western Japan, leading to the event. The results consistently indicate that a moist air mass near the Ryukyu Islands, which lies windward of the affected area, was transported by the Western Pacific Subtropical High in the lower troposphere. Observation system experiments were conducted to confirm the importance of windward information, and the resulting statistical verification showed degradation for precipitation forecasts that did not include windward observations. Furthermore, windspeed overestimation in the poor forecast resulted in the precipitation zone being pushed northward, and the weakened convergence led to weaker precipitation than that observed during the actual event.

Keywords windward region; sensitivity; ensemble; observation system experiments

1. Introduction

Heavy precipitation is common in the second half of the rainy season in Japan (usually from late June to July) because of the development of the Western Pacific Subtropical High (WPSH) and the transport of moist air masses by the southwest Asian monsoon. Research on improving the accuracy of numerical weather prediction (NWP) for torrential rain events (e.g., Kawabata et al. 2017; Otani et al. 2019) has been widely performed with the aim of mitigating serious disasters and economic losses due to heavy rain and associated flooding. The chaotic behavior of the atmosphere (e.g., Kawabata and Ueno 2020) means that predictions obtained using NWP depend strongly on the initial conditions, rendering it important that the accuracy of the initial values obtained is enhanced, with data assimilation being a possible means of attaining this goal. Recently, the assimilation of various observations resulted in improved forecasting for the Global Navigation Satellite System (GNSS), which retrieves precipitable water vapor (PWV; Seko et al. 2011; Shoji et al. 2009; Ikuta et al., 2022).

However, the density of the observation network was still insufficient for the NWP. Kato and Aranami (2005) investigated two cases of heavy rainfall during the rainy season in 2004, and by comparing the two forecasts with different accuracies, found that the poor forecast resulted from inaccuracies in the analysis of the wind velocity field, which determines the moist air trends in the lower atmosphere over the Sea of Japan. Yoshida et al. (2020) conducted observation system simulation experiments to assimilate simulated Raman Lidar (RL) pseudo-observation data into the windward region of a torrential rain event in 2014. The improved precipitation prediction accuracy associated with RL data assimilation was due to the positive impact of the background wind. In addition, Shoji et al. (2009) found the importance of propagating corrections downwind by assimilating PWV from GNSS and pointed out the importance of water vapor information in the windward region.

Previous studies have shown that assimilating new observations has yielded positive impacts in terms of prediction; however, the location of a new observation system and the optimization of the distribution of observations remain major research issues. Singular vectors (SVs) are frequently used to investigate these issues. For example, Yamaguchi et al. (2009) used SVs to show that assimilating dropwind-sonde observations improved the accuracy of typhoon track prediction in a region that was sensitive to the Global Ensemble Prediction System (GEPS) at the Japan Meteorological Agency (JMA). Ono et al. (2020) compared the structure of global-scale SVs with meso-scale SVs using GEPS and the Meso-scale Ensemble Prediction System (MEPS), which has been in operation since June 2019. Global SVs capture forecast uncertainties on a global scale, whereas meso SVs find uncertainties that are consistent in regional models on both spatial and temporal scales. Meso SVs are often detected in the lower atmosphere, particularly in the water vapor field. Another study that demonstrated the sensitivity of meso-scale convective systems by Yokota and Seko (2021) found that the first mode of the ensemble-based singular value represented the synoptic-scale front, with the 6^{th} mode indicating localized rain.

Scientifically, whether the sensitivity associated with linear analysis is consistent with the accuracy of predictions made using nonlinear models when new observations are assimilated into the sensitive region remains to be verified. In addition, even if a new observation system improves the accuracy of the analysis, in the case of strong winds, since improvements traveled over large distances within short periods, their impacts on predictions may be limited. Therefore, the purpose of this study is to comprehensively analyze the prediction accuracy by focusing on the relationship between the sensitive region and the positive impacts obtained through data assimilation.

In this study, the sensitivity of initial conditions for torrential rainfall forecasting was thus investigated from multiple perspectives using three methods, both linear and nonlinear. First, backward trajectory analysis was conducted, which was followed by ensemble sensitivity analysis, based on Enomoto et al. (2015), and finally, an observation system experiment (OSE), in which the observations in the sensitivity region were not assimilated, was conducted using the nonhydrostatic model (NHM) local ensemble transform Kalman filter (LETKF; Miyoshi and Aranami 2006; Kunii 2014).

The next section presents an overview of the heavy rainfall events that occurred in July 2018. Section 3 describes the method used to determine windward, sensitivity regions, and OSE configurations. Section 4 describes the results of the backward trajectory analysis, ensemble sensitivity analysis, and OSE, with a discussion of the sensitivity of the predictions for the unassimilated observations obtained using the ensemble–mean differences in the atmospheric distributions and ensemble correlations. Finally, the conclusions are presented in Section 5.

2. Case Description

Record-breaking heavy rainfall that caused notable damage to western Japan in early July 2018 was investigated in this study. Rainfall occurred under the influence of Typhoon Prapiroon (2018) and the Baiu front. The torrential rains were characterized by extraordinarily long-lasting precipitation, which continued for 48–72 h. Tsuguti et al. (2018) and Shimpo et al. (2019) suggested that three major factors contributed to the synoptic and meso-scale atmospheric circulation fields. The first was the persistence of two very moist air masses that entered western Japan, the second was the continual upwelling associated with activation of the Baiu front, and the third was the formation of a meso-scale line-shaped precipitation system. In this heavy rainfall event, the enhanced meridional temperature gradient, which resulted from the northerly airflow associated with Typhoon Prapiroon (2018) and the Okhotsk High over the Sea of Japan, contributed to the persistence of the Baiu front (Enomoto 2019; Moteki 2019). In this study, the analysis period was set from 00 UTC on 5 July to 12 UTC on 6 July, which includes the peak of the heavy rainfall event. Figure 1 shows the mean sea-level pressure obtained using JMA meso-analysis (JMA 2019) and the accumulated precipitation observed by the radar-rain gauge precipitation analysis (R/A) system from JMA during the validation period. Precipitation of 150–200 mm or more was observed over a wide area during the analysis period, indicating that southwesterly airflow from the East China Sea moved toward western Japan along the edge of the enhanced WPSH during this period.

3. Data and Methods

3.1 Backward trajectory analysis

Backward trajectory analysis was conducted using a modified version of the volcanic ash tracking model (PUFF; Tanaka 1994) to clarify the windward region of the torrential rain. The PUFF model was originally used to calculate the locations of volcanic ash under conditions of transportation, free fall, and diffusion. In this study, air masses were placed at arbitrary locations and their past locations were calculated. Neither free fall nor diffusion was considered. Meso-analysis data from the JMA were used to drive the PUFF model. The data set provides information every 3 h; however, because the temporal variability of vertical wind is microscopic in nature, only horizontal winds were included in this study, meaning that the data required careful handling. Cubic spline interpolation was used for both temporal and spatial enhancement, allowing the grid spacing to be reduced from 5 to 2.5 km and the time interval to be improved from 3 h to 90 min. Linear interpolation was then applied in 5-min steps using the Euler scheme. The trajectories were calculated from 40 randomly selected locations in western Japan at heights of 1000, 2000, and 3000 m. The initial backward calculations were conducted for 00 and 12 UTC on the 6th of July, after which data were generated for each successive 24 h or until the trajectory reached the lateral boundary of the analysis domain.

3.2 Ensemble-based sensitivity analysis

a. Method

An ensemble SV sensitivity analysis (EnSVSA) based on Enomoto et al. (2015) was conducted to determine the verification time and domain of the initial disturbances with high sensitivity. This method is consistent with the adjoint-based SV methods used for linear cases with infinite ensemble members. A brief description of this method is as follows.

The time evolution of state vector x with dimension n was generated using a nonlinear model $M(x)$. For an ensemble forecast that includes m members with perturbation y_i, disturbance z_i at the initial time can be obtained as follows:

$$z_i = M(x + y_i) - M(x), i = 1,2,\cdots,m.\#(1)$$

Assuming a linear evolution of the initial perturbation, sensitivity analysis is used to find the optimal coefficient $\boldsymbol{p}$ for the linear combination of the members in the verification domain, which demonstrates the largest range of perturbations at the verification time. The corresponding perturbations at the verification time t are as follows:

$$\mathbf{z} = \boldsymbol{p}_1\boldsymbol{z}_1 + \boldsymbol{p}_2\boldsymbol{z}_2 + \cdots + \boldsymbol{p}_{\mathrm{m}}\boldsymbol{z}_m,\#(2)$$

$$\mathbf{p}^{\top} = (\boldsymbol{p}_1,\boldsymbol{p}_2,\cdots,\boldsymbol{p}_{\mathrm{m}}).\#(3)$$

Using the coefficient p, the initial perturbation that corresponds to the perturbation with the highest growth in spread at the verification time is obtained using:

$$\mathbf{y} = \boldsymbol{p}_1\boldsymbol{y}_1 + \boldsymbol{p}_2\boldsymbol{y}_2 + \cdots + \boldsymbol{p}_{\mathrm{m}}\boldsymbol{y}_{m.}\#(4)$$

The ensemble perturbations at the initial and verification times are then represented by the matrixes:

$$\boldsymbol{Y} = (\boldsymbol{y}_1,\boldsymbol{y}_2,\cdots,\boldsymbol{y}_m),\ \boldsymbol{Z} = (\boldsymbol{z}_1,\boldsymbol{z}_2,\cdots,\boldsymbol{z}_m),\#(5)$$

respectively.

We find that the vector $\boldsymbol{p}$ maximizes the norm $\|\boldsymbol{Zp}\| = \sqrt{\boldsymbol{p}^{\top}\boldsymbol{Z}^{\top}\boldsymbol{GZp}}$ under the constraint $\|\boldsymbol{y}\| = \sqrt{\boldsymbol{p}^{\top}\boldsymbol{Y}^{\top}\boldsymbol{GYp}} = 1$, if the same energy norm is denoted by the diagonal matrix $\boldsymbol{G}$ for both norms. This solution can be obtained using the undetermined Lagrange multiplier method with the Lagrange function, expressed as follows:

$$L(\boldsymbol{p},\lambda) = \boldsymbol{p}^{\top}\boldsymbol{Z}^{\top}\boldsymbol{GZp} + \lambda(\mathbf{1} - \boldsymbol{p}^{\top}\boldsymbol{Y}^{\top}\boldsymbol{GYp}).\#(6)$$

Taking the partial differentiation with respect to p in Eq. (6), the following generalized eigenvalue problem is obtained:

$$\frac{\partial L(\boldsymbol{p},\lambda)}{\partial \boldsymbol{p}} = 2\boldsymbol{Z}^{\top}\boldsymbol{GZp} - 2\boldsymbol{\lambda}\boldsymbol{Y}^{\top}\boldsymbol{GYp} = 0,\#(7)$$

$$(\boldsymbol{Y}^{\top}\boldsymbol{GY})^{-\mathbf{1}}(\boldsymbol{Z}^{\top}\boldsymbol{GZ})\boldsymbol{p} = \lambda\boldsymbol{p},\#(8)$$

where the diagonal elements of the matrix λ are eigenvalues. The dimension of the $(\boldsymbol{Y}^{\top}\boldsymbol{GY})^{-1}\boldsymbol{Z}^{\top}\boldsymbol{GZ}$ matrix in Eq. (8) is $m \times m$, where m is equal to the ensemble size [$\sim O(10)$]. Thus, this eigenvalue problem can be easily solved. Note that to simplify problem (8), Enomoto et al. (2015), suggested selecting an orthonormal set of initial perturbations that result in $\boldsymbol{Y}^{\top}\boldsymbol{GY}$ as the identity matrix, which results in (8) becoming an eigenvalue problem for $\boldsymbol{Z}^{\top}\boldsymbol{GZ}$. This assumption was made only for perturbations obtained using the SV method (see Section 3.2b).

Enomoto et al. (2015) formulated an EnSVSA under finite member approximation using 25 members of a global ensemble, which had only 12 modes of freedom due to the positively and negatively perturbed members included as SVs. Thus, they investigated the first 10 modes at most. Matsueda et al. (2011) limited the validation period to 120 h under the consideration of linear error growth. Following the methods used previously, we limited the validation period to 24 h and investigated the first leading mode under nonlinear error growth and a finite number of freedoms. An additional purpose of this study was to demonstrate the availability of EnSVSA for use in this case by comparing it with backward trajectory analysis and OSE.

b. Sensitivity analysis

This case is unique because its major forcing was the result of the synoptic scale, as suggested by Tsuguti et al. (2018) and Matsunobu and Matsueda (2019). Because global and regional models deal with data at different temporal and spatial scales, the sensitivity analyses in this study were conducted using data from both models while considering the characteristics of the actual rainfall event. NHM-LETKF (CTRL; see Section 3.3) was used as the regional model, and the weekly global ensemble forecast from the European Centre for Medium-Range Weather Forecasts (ECMWF) was used as the global model for the sensitivity analysis. The initial perturbations in the CTRL and ECMWF data were obtained using the LETKF and SVs, respectively. Since all 51 of the ensemble members were created using LETKF, the initial perturbations in the CTRL were independent of each other. However, the initial perturbations of the ECMWF were not independent because pairs of positive and negative pairs were used to create the total; therefore, only 27 independent members were utilized in the control run and positive perturbations used in this study.

The method used assumes that the initial disturbance grows linearly, meaning that this method cannot be used for long-term analysis in which nonlinear growth dominates. For example, Matsueda et al. (2011) assumed linear growth for a 120-h verification period in their sensitivity analysis that used the blocking high as a target case. Essentially, the perturbation growth rate in the NWPs of torrential rainfall cases, in which convective processes dominate, increases to become greater than that observed in global-scale phenomena. In this study, however, the perturbation growth rate of the NWP was assumed to be linear over 24 h in both the global and regional models, because forcing at the synoptic scale dominated during the torrential rain event.

Validation time was performed for the period 12 UTC on 6 July (24 hours after the start of the study period at 12 UTC on 5 July). The moist total energy (MTE) norm (Barkmeijer et al. 2001, J kg^{-1}) was used for the evaluation and was calculated using the following:

$$MTE = \frac{1}{2A}\iint A\left[u'^2 + v'^2 + \frac{C_p}{T_r}T'^2 + w_q\frac{L_c^2}{C_pT_r}q'^2 + RT_r\left(\frac{p_s'}{p_r}\right)^2\right]dpdA, \#(9)$$

where $u',\ v',\ T',\ q',\ and\ p_s'$ represent the perturbations in the basic fields, which were provided from the control simulation by ECMWF and the ensemble mean by CTRL, respectively, of the zonal and meridional winds (m s^{-1}), air temperature (K), specific humidity (kg kg^{-1}), and surface pressure (hPa), respectively. The zonal and meridional winds represent the kinetic energy, the air temperature and surface pressure represent the potential energy, and the specific humidity represents the energy of the water vapor. The specific heat at constant pressure is C_p= 1,005.7 (J kg^{-1} K^{-1}), gas constant of dry air is R = 287.04 (J kg K^{-1}), and latent heat for the evaporation of water is L_c = 2.51 × 10^6 (J kg^{-1}). The reference temperature was T_r= 270 (K), and the reference pressure was p_r = 1,000 (hPa). w_q is the weight of the specific humidity. In this study, weights of 0.6 and 0.5 were used as the global and meso SVs respectively, following Saito et al. (2011).

3.3 Observation system experiment

Two analysis systems with horizontal resolutions of 15 and 5 km and one forecast system with a 5 km grid spacing (Fig. 2a) were used in the study. First, the NHM-LETKF with a 15 km grid spacing and 50 vertical layers (15 km-LETKF) was run from 12 UTC on 3 July (Fig. 2b; black box). The initial and boundary conditions were obtained from the operational meso-scale and global forecasts data provided by the JMA, respectively, and perturbations were obtained from the 51 members in the operational global ensemble system. The hourly observations were assimilated every six hours. Temperature, pressure, horizontal wind, PWV, relative humidity, and raindrop Doppler velocity were obtained using conventional observations (e.g., surface observations, ships, buoys, radiosondes, aircraft, wind profilers, radar, GNSS, microwave scatterometers, and visible/infrared imagers). The CTRL was then run using NHM-LETKF with a horizontal resolution of 5 km (5km-LETKF) by downscaling the analysis of the 15km-LETKF from 00 UTC on July 5 as the initial and boundary conditions (Fig. 2b; red box). All the available observations were assimilated into the LETKF system at both 15 and 5 kms because the 15km-LETKF and 5km-LETKF are expected to result in better boundary and initial conditions than the ensemble simulations without any data assimilation. The experimental area was set to consider the Okhotsk High over the Sea of Japan (see Section 2), and a 24-h extended forecast was obtained using the CTRL (CTRL forecast), with the domain wide enough to cover both the moist airflow from the south and the cold airflow from the north over western Japan. The boundary conditions for the extended forecast were obtained from the JMA Operational Global Model. A data denial experiment (DNL) was then performed as an OSE with some observations between 06 and 12 UTC on July 5. A 24-h extended forecast (DNL forecast) was thus conducted at 12 UTC.

The ensemble means of the results from each experimental system were compared, and the meso-analysis and R/A data from the JMA were used for validation. Fraction skill scores (FSS) (Roberts and Lean 2008; Duc et al. 2013), threat scores (TS), and bias scores (BS) were used to evaluate the accuracy of the forecast. The TS and BS are defined as:

$$TS = \frac{FO}{FO + FX + XO}, BS = \frac{FO + FX}{FO + XO}, \#(10)$$

where FO, FX, and XO are the number of hit, miss, and false grid points, respectively. The FSS is defined as:

$$FSS = 1 - \frac{\frac{1}{n}\sum_1^n (P_{fcst} - P_{obs})^2}{\frac{1}{n}\sum_1^n (P_{fcst})^2 + \frac{1}{n}\sum_1^n (P_{obs})^2} \#(11)$$

where P_{fcst}, P_{obs}, and n represent the number of forecast, observed, and total grids in the verification domains, respectively.

4. Results

4.1 Backward trajectory analysis

Figure 3 shows the backward trajectory analysis that was calculated at heights of 1000, 2000, and 3000 m in the area in which the heavy rainfall occurred at 00 and 12 UTC on 6 July. The lower atmosphere air masses at that reached western Japan at 25°N and 130°E traveled for 12 h before arriving in western Japan and were mainly determined by the south–southwest airflow. The analysis showed that the airflow entering northern Kyushu was south–southwesterly at 00 UTC (Fig. 3a) and southwesterly at 12 UTC (Fig. 3d), with the westerly wind component at the north edge of the WPSH. Figure 3 suggests that omitting the vertical motion from this calculation would not substantially change the results obtained because the trajectories were mostly the same at different heights. Although the front was over western Japan at this time (Fig. 1), this area was the final destination and the vertical motion of the air mass over the entire trajectory was hardly affected.

4.2 Ensemble sensitivity analysis

The MTE in Eq. 9 was first calculated over the validation regions as the evaluation norm, followed by p in Eq. 8 as the sensitivity to the norm. The sensitivity evaluation allowed for the initial perturbation Y (Eq. 5), to be reproduced as y (Eq. 4) over the entire experimental domain. Figures 4a and 4b show the sensitivities calculated using the CTRL and ECMWF data, normalized to the range of 0–1. The red boxes indicating the validation regions used in each ensemble sensitivity analysis are not exactly the same because the CTRL was calculated using LETKF with a 5-km horizontal grid spacing while the ECMWF was obtained at 16 km. Figure 4c shows the ensemble sensitivity of CTRL, not for the MTE, but for the zonal and meridional winds (m s^{-1}), temperature (K), specific humidity (kg kg^{-1}), and surface pressure (hPa), which were normalized to the maximum MTE value in Eq. 9. The SVs obtained for regional models can be spatially localized into narrow areas and can include extremely large values (e.g., Kunii 2010), as in SR2. Thus, all values of 0–50 were normalized to 0–1 and values larger than 50 were set to 1. A common high-sensitivity region (SR1) was observed at approximately 25°N and 127°E (Figs. 4a and 4b) in both sensitivity analyses, which corresponds to the windward side of the inflow path observed in the backward trajectory analysis (Fig. 3). Another high-sensitivity region (SR2) around 40°N and 120°E appeared only in the CTRL but not in the ECMWF data. For the CTRL, since the lateral boundary conditions were obtained using 15km-LETKF, the area was contaminated by 15km-LETKF for a few hours after initiation, and interference between the fine and coarse models was common. Therefore, this result was assumed to be unreliable in this study. The energy norm (Fig. 4c) was then decomposed to investigate the meteorological elements that dominate the high-sensitivity region of SR1. The kinetic energy of the zonal and meridional winds is concentrated along the edge of the WPSH, similar to the total value field. However, the temperature is less concentrated along the WPSH, and the distribution of the sensitivity of water vapor appears to be generally sporadic rather than systematic, in the same manner as kinetic energy. Other sensitive regions that would affect the sensitivity in the verification area (120°E, 34°N and 140°E, 25°N) can also be seen in both Figs. 4a and 4b; however, these regions are excluded from the following discussion because it is clear that only SR1 relates to the windward region from our backward trajectory analysis.

4.3 Observation system experiment

The results for the windward (Section 4.1) and sensitivity regions (Section 4.2) indicate that the region with the largest impact on the precipitation system in this study lies in the vicinity of the Okinawa Islands and corresponds to the windward side of the heavy rainfall area. Therefore, the DNL was conducted, in which the observation data in the not-assimilated-observation box (NOB) for the regions 22°N–27°N and 125°E–135°E are ignored (Fig. 5). The NOB area was set considering SR1 and the windward region specified in Fig. 3. Most of the unassimilated data are distributed near the surface, and no data is available above an altitude of 2,000 m, for both the CTRL and the DNL.

a. Impact on the analysis

Because the density of observations differs for the western and eastern parts of the NOB, the impact of the OSE was investigated by further splitting the NOB into western and eastern areas. The vertical profiles obtained using the CTRL, DNL, and JMA meso-analysis are shown in Fig. 6, together with the differences between the JMA meso-analysis and the CTRL or DNL for each meteorological element in the western NOB at 12 UTC on July 5. Below 850 hPa, the meridional velocity in the DNL is stronger than that in CTRL, with the maximum difference reaching 2 m s^{-1}. Below 900 hPa, the temperature in the DNL is 1 K lower and the specific humidity 1 g kg^{-1} lower than that in the CTRL. The differences are not as large in the eastern NOB as observed in the western validation region; however, the wind speeds are approximately 0.5 m s^{-1} higher in the lower atmosphere in the DNL as compared to those observed in the western region (not shown).

b. Forecast accuracy for precipitation

The accumulated precipitation for 12 h from 00 to 11 UTC on July 6 in CTRL (CTRL forecast) and DNL (DNL forecast) are shown in Fig. 7. This time period was determined using the results of the backward trajectory analysis, which indicated that it took 12 h for the air mass in the NOB to enter the precipitation area. Validation of these precipitation predictions was conducted over the Setouchi area (the black box in the figure), as the inflow from the NOB continued in this area during the studied time period, although precipitation was also observed over northern Kyushu during the R/A observation at this time. Setouchi was selected because the backward trajectory showed that the air mass reaching Setouchi originated from the NOB, whereas the air mass observed in northern Kyushu was likely from elsewhere (Fig. 3).

The precipitation systems obtained by R/A, CTRL, and DNL were generally comparable, although the direction in which the rain system travels differed slightly. However, less precipitation was observed over Setouchi in the DNL (Fig. 7d) than that in the CTRL. This is confirmed by the validation scores (Table 1), which show that the FSS is significantly smaller in the DNL than it is in the CTRL for precipitation thresholds of 85 and 100 mm, with FSSs of 0.42 and 0.18 obtained by CRTL and DNL, respectively, for a precipitation threshold of 100 mm and validation grid size of 30 km. These results indicate an improvement rate of 1.3 in the FSS of the CTRL. The FSSs for weak and moderate rains in CTRL and DNL were mostly the same; however, those for intense rains were worse in DNL than in CTRL. The BSs in the CTRL and DNL were almost identical at low thresholds, whereas the DNL resulted in a significant underestimation for larger thresholds.

4.4 Windward and sensitivity regions

Matsunobu and Matsueda (2019) discussed the predictability of the same torrential rainfall event using a medium-term forecast, and the results indicated that the overhang of the WPSH had a significant impact on prediction accuracy. Sekizawa et al. (2019) and Takemura et al. (2019) analyzed the divergence of the vertically integrated water vapor flux during the event, and demonstrated that the event was mainly due to extremely large anomalies in the wind field and that the convective activities over the East China Sea contributed to the persistence of the southwesterly flow.

It is believed that the windward (see Section 4.1) and sensitivity regions (see Section 4.2) are not always located in the same area in most torrential rain cases. In the studied rainfall event, the windward and sensitivity regions were considered to have been in the same area because of the strong influence of the unusually moist southwesterly airflow. Ono et al. (2020) also investigated the same case and showed that the high-sensitivity region calculated using the meso SVs lay over the sea south of Japan, which coincides with the windward region of the moist airflow in this study. Furthermore, the sensitive region calculated using the global SVs showed three peaks, one on the eastern coast of China, one in northern Japan, and the other southeast of the Japanese islands. The global SVs from the JMA showed different sensitivity distributions compared to those in the ECMWF, which is probably because these two systems differ in terms of factors such as resolution and validation time. The agreement between the meso and global SVs in this study supports the finding that SR1 was a highly sensitive region during the analysis period.

As explained above, backward trajectories and ensemble sensitivity analyses are considered quantitatively consistent because they represent different wind and energy elements, respectively. These analyses show similar paths, with little difference observed over time.

4.5 Impact of the windward region on the precipitation forecast

The root mean square difference (RMSD) indicates a less accurate precipitation prediction for the DNL than the CTRL, which is due to the lack of assimilation of some observations (Fig. 8). The obtained RMSDs were integrated for all vertical layers and normalized to a maximum value of 1 for ease of comparison.

The zonal (Fig. 8a), meridional (Fig. 8b), divergence (Fig. 8c), and vorticity (Fig. 8d) results all showed maxima in the northwestern part of the NOB and reached western Japan from this area. In particular, a significant signal was observed for meridional winds and divergence in western Japan. Therefore, rejecting some of the observations degraded the accuracy of the precipitation prediction over the area from the NOB to the verification region. It would be useful to point out that the locations of these degraded areas are consistent with the results of the back trajectory analysis (Fig. 3) and the airflow along the WPSH (Fig. 1). These facts suggest that the change in precipitation prediction was due to low-level winds that were dominated by synoptic-scale pressure systems.

In addition, the different results in the DNL and CTRL for the lower atmosphere were averaged to those below 900 hPa (Fig. 9). The results for each element were relatively large in comparison with their absolute values, especially in the Setouchi area, where the accuracies of the precipitation forecast in the DNL and CNTL differ considerably (see Fig. 7). In particular, the southerly winds in the CTRL were stronger than those from the DNL (Fig. 9b), resulting in a more northerly precipitation system.

In addition,, both divergence and vorticity (Figs. 9c and 9d) were weaker in the DNL than in the CTRL, indicating weaker convergence in the low troposphere and a stronger anticyclonic component in the DNL. These facts indicate that the difference impacted the precipitation prediction during the latter 12 h of the validation period (Fig. 9).

This study focused extensively on the wind field because the decomposition of the evaluation norm in the sensitive region (described in Section 4.2) indicated that the kinetic energy of the zonal and meridional winds was concentrated along the edge of the WPSH, as was the total value field. Similarly, the difference in the results obtained from the DNL and CTRL for the specific humidity was not as pronounced as that seen in the wind field (not shown). These results support those obtained in previous studies in that the wind velocity field promoted by atmospheric circulation on the synoptic scale is important in this torrential rainfall event. The fact that the DNL prediction accuracy for large precipitation thresholds was worse than that in the CTRL supports this conclusion and suggests that the synoptic field was the dominant factor in torrential rainfall. In a previous study related to the same event, Ono et al. (2020) showed a decrease in the Brier skill scores in the probabilistic forecasts for 3 h of accumulated precipitation by removing the ensemble perturbations at the meso-scale from the operational meso-scale ensemble prediction system. This result also suggests that information from unassimilated observations is important for understanding the formation mechanism and structure of strong precipitation systems.

To investigate the relationship between the wind field and precipitation accuracy indeces, ensemble correlations are shown in Fig. 10. This investigation was conducted with the region in the black box shown in Fig. 7. The scatter plots for BS and meridional wind speed (Fig. 10a) show that the weaker the southerly component of the low-level meridional wind, the smaller the BS. The scatter plots of the TS and divergence at 900 hPa (Fig. 10b) show that the higher the divergence component, the smaller the TS. Both of the correlations in these relationshps were relatively high at −0.59. In addition, the CTRL (red) is mostly distributed in the upper region of Fig. 10 as compared to the DNL, which is due to the difference in the wind speeds in the CTRL and DNL.

Finally, we clarified that differences in the initial conditions led to different prediction abilities (Fig. 11). The ensemble mean of water vapor along the WPSH in the CTRL was much greater than that in the DNL (Figs. 11a and b). This indicates that improving the precipitation forecast was mainly achieved by allowing wind to flow along the WPSH. Moreover, increased amounts of atmospheric water vapor led to increased precipitation, even though no distinct structure was observed in water vapor sensitivity (Fig. 4c). The spread at the initiatial conditions of the OSE (Figs. 11c and d) indicates that the analysis error along the path of the air mass in the DNL is greater than that in the CTRL, suggesting that the larger error affected the precipitation forecast made using the DNL.

5. Discussion and Conclusion

This study is a comprehensive investigation of the sensitivity of numerical prediction for the heavy rainfall that occurred in western Japan in early July 2018.

First, backward trajectory analysis confirmed the origin of the air masses that reached western Japan, where the heavy rainfall occurred, as a 12-h long south–southwest airflow.

Second, ensemble sensitivity analysis showed that both the NHM-LETKF and the weekly global ensemble forecast from the ECMWF were highly sensitive in the region around 25°N, 130°E, which corresponds to the windward region obtained using backward trajectory analysis. This seems to have been caused by the Pacific High and moist soutwesterly airflow from the East China Sea. To confirm this, the total energy norm was decomposed with each component, with results showing that the kinetic energy of the zonal and meridional winds was concentrated, together with the total value field, along the edge of the WPSH, while the others were not. This suggests that the wind was dominant during the heavy rainfall event. The windward and sensitive regions did not always appear in the same area, and the results suggested that the airflow observed in the backward trajectory passed through the sensitive region.

Third, to show the importance of windward information, the OSE was conducted with (CTRL) and without (DNL) observations in the windward region. The DNL experiment overestimated the wind speeds in the lower atmosphere compared with the observations. As a result, the CTRL experiment was more accurate than the DNL experiment in predicting the torrential rainfall. Therefore, it was concluded that the difference between the DNL and CTRL experiments was affected by the wind along the WPSH and extended to the heavy rainfall zone. Statistical verification showed that the precipitation forecast obtained by the DNL was degraded owing to the lack of windward observations. The overestimation of the wind speeds in the poor forecast suggested that the precipitation zone was further northward than it actually was, weakening the convergence and leading to an inferior precipitation prediction.

The air mass was advected into the heavy area located to the south of the analysis domain before 24 h had passed, as shown in Fig. 3, while the sensitivity (SR1) lay in a 12-h area around Okinawa islands. Therefore, the sensitivity was not directly linked to the air mass. The decomposition of the energy norm in the ensemble sensitivity indicates that the sensitivity was mainly affected by the dynamic (wind) field. It is likely that the air mass traveled and passed through the SR1 region approximately 12 h before the rainfall event, as confirmed by the OSE, in which the air mass decelerated in the CTRL but not in the DNL. In addition, large amounts of water vapor were advected along the WPSH in the CTRL, as shown in Fig. 11. These factors improved the prediction accuracy.

We clarified that all the three methods; backward trajectory analysis and ensemble sensitivity analysis as linear methods, and the OSE as a nonlinear method, indicate the common region affecting torrential rain. This suggests that the event was dominated by a linear process, with synoptic forcing along the WPSH affecting wind. However, such results are likely to be obtained for meso-scale phenomena with strong nonlinearity. Therefore, similar analyses should be conducted for different cases in the future.

Data Availability Statement

The output data from this study were archived and are available upon request from the corresponding author. The observational data and data assimilation system are available under contract with the Japan Meteorological Agency, because the data are basically collected and developed for the operational purpose.

Acknowledgment

The authors thank Drs. Seko, Sawada, Hotta, Ikuta, Kondo, Matsueda, Le Duc, and P. -Y. Wu for their valuable comments, and deeply appreciate two anonymous reviewers and the editor for their great efforts on improving this manuscript. This study was partly supported by Grant-in-Aid for Scientific Research; "Study on uncertainty of cumulonimbus initiation and development using particle filter" (17H02962), "Investigation of Heavy Rainfall Mechanism by Mathematical Statistics Using Large Ensemble" (23KF0161), "Study on Initial Perturbations Reflecting Analysis Error and Growing modes for Ensemble Prediction of Linear-shaped Rain Bands" (23K03498), ROIS-DS-JOINT2023; "Understanding meteorological phenomena using ensemble predictions" (026RP2023), the Fugaku project by MEXT (JPMXP1020200305); the "Large Ensemble Atmospheric and Environmental Prediction for Disaster Prevention and Mitigation" (ID:hp200128, hp210166, hp220167), and cooperative research between the University of Tsukuba and the Meteorological Research Institute.

References

Barkmeijer, J., R. Buizza, T. N. Palmer, K. Puri, and J.-F. Mahfouf, 2001: Tropical singular vectors computed with linearized diabatic physics. *Quart. J. Royal Meteor. Soc.*, **127**, 685-708.

Duc, L., K. Saito, and H. Seko, 2013: Spatial-temporal fractions verification for high-resolution ensemble forecasts. *Tellus A*, **65**, 1, doi:10.3402/tellusa.v65i0.18171.

Enomoto, T., S. Yamane, and W. Ohfuchi, 2015: Simple sensitivity analysis using ensemble forecasts. *J. Meteorol. Soc. Japn*, **93**, 199-213.

Enomoto, T., 2019: Influence of the track forecast of Typhoon Prapiroon on the heavy rainfall in western Japan in July 2018. *Sola*, **15A**, 66-71, doi:10.2151/sola.15A-012.

Ikuta, Y., H. Seko, Y. Shoji, 2022: Assimilation of shipborne precipitable water vapour by Global Navigation Satellite Systems for extreme precipitation events, *Q. J. R. Meteorol. Soc.*, **148**, 57-75, doi:10.1002/qj.4192

Kato, T., and K. Aranami, 2005: Formation factors of 2004 Niigata-Fukushima and Fukui heavy rainfalls and problems in the predictions using a cloud-resolving model. *Sola*, **1**, 1-4, doi:10.2151/sola.2005-001.

Kawabata, T., H. Iwai, H. Seko, Y. Shoji, K. Saito, S. Ishii, and K. Mizutani, 2014: Cloud-resolving 4D-Var assimilation of Doppler wind lidar data on a meso-gamma-scale convective system. *Mon. Wea, Rev.*, **142**, 4484-4498.

Kawabata, T., and G. Ueno, 2020: Non-gaussian probability densities of convection initiation and development investigated using a particle filter with a storm-scale numerical weather prediction model. *Mon. Wea, Rev.*, **148**, 3-20, doi:10.1175/MWR-D-18-0367.1.

Kunii, M., 2010: MSV method. *Technical Report of the Meteorological Research Institute*, **62**, 73-77, doi:10.11483/mritechrepo.62.

Kunii, M., 2014: Mesoscale data assimilation for a local severe rainfall event with the NHM-LETKF system. *Weather Forecasting*, **29**, 1093-1105.

Matsueda, M., Z. Kyoda, H. L. T. Toth, and T. Tsuyuki, 2011: Predictability of atmospheric blocking event that occurred on 15 December 2005. *Mon. Wea, Rev.*, **139**, 2455-2470.

Matsunobu, T., and M. Matsueda, 2019: Assessing the predictability of heavy rainfall events in Japan in early July 2018 on medium-range timescales. *Sola*, **15A**, 19-24, doi:10.2151/sola.15A-004.

Miyoshi, T., and K. Aranami, 2006: Applying a four-dimensional local ensemble transform Kalman filter (4D-LETKF) to the JMA nonhydrostatic model (NHM). *Sola*, **2**, 128-131, doi:10.2151/sola.2006-033.

Moteki, Q., 2019: Role of Typhoon Prapiroon (Typhoon No. 7) on the formation process of the Baiu front inducing heavy rain in July 2018 in western Japan. *Sola*, **15A**, 37-42, doi:10.2151/sola.15A-007.

Ono, K., M. Kunii, and Y. Honda, 2021: The regional model-based mesoscalemesoscale ensemble prediction system, MEPS, at the Japan meteorological agency. *Q. J. R. Meteorol. Soc.*, **147**, 465-484, doi:10.1002/qj.3928.

Otani, S., N. Nakada, A. Isimoto, C. Akieda, N. Kazahaya, Y. Nishimori, T. Nakamura, Y. Yorioka, T. Tatsukami, T. Iwata, H. Seko, and S. Yokota, 2019: Analysis on the relation between the heavy rainfall and its environment, especially low-level inflow, obtained by the ensemble forecast experiments. *Tenki*, **66**, 141-160 (in Japanese).

Roberts, N. M., and H. W. Lean, 2008: Scale-selective verification of rainfall accumulations from high-resolution forecasts of convective events. *Mon. Wea. Rev.*, **136**, 78-97.

Saito, K., M. Hara, M. Kunii, H. Seko, and M. Yamaguchi, 2011: Comparison of initial perturbation methods for the mesoscale ensemble prediction system of the Meteorological Research Institute for the WWRP Beijing 2008 Olympics Research and Development Project (B08RDP). *Tellus A*, **63**, 445-467, doi:10.1111/j.1600-0870.2010.00509.x.

Sekizawa, S., T. Miyasaka, H. Nakamura, A. Shimpo, K. Takemura, and S. Maeda, 2019: Anomalous moisture transport and oceanic evaporation during a torrential rainfall event over western Japan in early July 2018. *Sola*, **15A**, 25-30, doi:10.2151/sola.15A-005.

Seko, H., T. Miyoshi, Y. Shoji, and K. Saito, 2011: Data assimilation experiments of precipitable water vapour using the LETKF system: intense rainfall event over Japan 28 July 2008. *Tellus A*, **63**, 402-412.

Shoji, Y., M. Kunii, and K. Saito, 2009: Assimilation of nationwide and global GPS PWV data on heavy rainfall in the 28 July 2008 Hokuriku and Kinki, Japan. *Sola*, **5**, 45-48.

Takemura, K., S. Wakamatsu, H. Togawa, A. Shimpo, C. Kobayashi, S. Maeda, and H. Nakamura, 2019: Extreme moisture flux convergence over western Japan during the heavy rain event of July 2018. *Sola*, **15A**, 49-54.

Tanaka, H. L., 1994: Development of a prediction scheme for volcanic ash fall from Redoubt volcano, Alaska, Proc. First International Symposium on Volcanic Ash and Aviation Safety. *U.S Geol. Surv. Bull.*, **2047**, 283-291.

Tsuguti, H., N. Seino, H. Kawase, Y. Imada, T. Nakaegawa, and I. Takayabu, 2019: Meteorological overview and mesoscale characteristics of the heavy rain event of July 2018 in Japan. *Landslides*, **16**, 363-371.

Yamaguchi, M., T. Iriguchi, T. Nakazawa, and C.-C. Wu, 2009: An observing system experiment of Typhoon Conson (2004) using a singular vector method and DOTSTAR data. *Mon. Wea, Rev.*, **137**, 2801-2816.

Yokota, S., and H. Seko, 2021: Ensemble-based singular value decomposition analysis to clarify the causes of heavy rainfall. *Q. J. R. Meteorol. Soc.*, **147**, 2244-2263, doi:10.1002/qj.4020.

Yoshida, S., S. Yokota, H. Seko, T. Sakai, and T. Nagai, 2020: Observation system simulation experiments of water vapor profiles observed by Raman Lidar using LETKF system. *Sola*, **16**, 43-50, doi:10.2151/sola.2020-008.

List of Figures

Fig. 1 Average sea-level pressure (contour intervals: 2 hPa) from the JMA meso-analysis and accumulated precipitation [shade: mm (36 h)$^{-1}$] from the JMA R/A system for the period 00 UTC on July 5 to 12 UTC on July 6.

Fig. 2 (a) Experimental time sequence, (b) calculation domain, and (c) setting.

Fig. 3 Backward trajectory analysis over 24 h at heights of 1000 (a and d), 2000 (b and e), and 3000 m (c and g), starting over the rainfall area in western Japan. White circles indicate the initial coordinates, and the colors in each trajectory indicate the elapsed time.

Fig. 4 Ensemble sensitivity of y in Eq. 4 for (a) CTRL and (b) ECMWF at 12 UTC on July 6. Verification area is western Japan (red box). Contours in (a) and (b) denote heights associated with 925-hPa in 50-m intervals. SR1 and SR2 areas (black boxes) are explained in the text. (c) Components of the 5km-LETKF-CTRL sensitivity: zonal wind (upper left), meridional wind (upper center), temperature (upper right), specific humidity (bottom left), and surface pressure (bottom center).

Fig. 5 Distribution of observations excluded from the DNL experiment. The boundary splitting the eastern and western parts of the NOB lies at approximately 130°E. Red, blue, green, purple, and gray indicate the temperature, wind speed, height, specific humidity, and precipitable water, respectively.

Fig. 6 Vertical profiles obtained using CTRL (blue), DNL (red), JMA meso-analysis (black) (upper), and the difference between the results obtained by CTRL (blue) and DNL (red) minus the meso-analysis (lower) at 12 UTC on July 5, averaged over the western part of the NOB.

Fig. 7 Accumulated precipitation for 12 h from 00 to 12 UTC on July 6. The (a) R/A, (b) CTRL, (c) DNL predicted rainfall, and (d) DNL minus CTRL. The black box (Setouchi) represents the verification area for the FSS, TS, and BS.

Fig. 8 RMSD of the CTRL and DNL forecasts from 12 UTC on July 5 to 12 UTC on July 6: (a) zonal wind, (b) meridional wind, (c) divergence, and (d) vorticity, normalized to a maximum value of 1. The black dotted box indicates NOB.

Fig. 9 Differences in the accumulated rainfall over 12 h in the CNTL and DNL (DNL minus CTRL) forecasts, and averaged below 900 hPa from 00 to 12 UTC on July 6: (a) zonal wind, (b) meridional wind, (c) divergence, and (d) vorticity.

Fig. 10 (a) Scatter plots of the BSs to the 100 mm threshold and the averaged meridional wind below 900 hPa, and (b) the TSs to the 100 mm threshold and the averaged diver-gence at 900 hPa from 00 to 12 UTC on July 6. The calculation domain is represented by the black box in Fig.7. Red (blue) points illustrate each ensemble member of the CTRL forecast (DNL forecast). The black line represents first-order approximation line.

Fig. 11 Ensemble mean (upper) and spread (lower) of mixing ratio of water vapor at 925 hPa, 12 UTC 5 July 2018 (left column: CTRL, right: DNL).

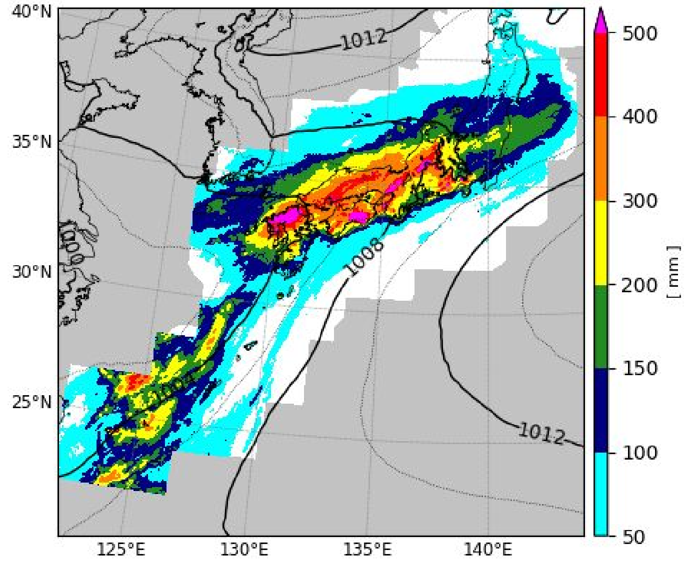

Fig. 1 Average sea-level pressure (contour intervals: 2 hPa) from the JMA meso-analysis and accumulated precipitation [shade: mm (36 h)$^{-1}$] from the JMA R/A system for the period 00 UTC on July 5 to 12 UTC on July 6.

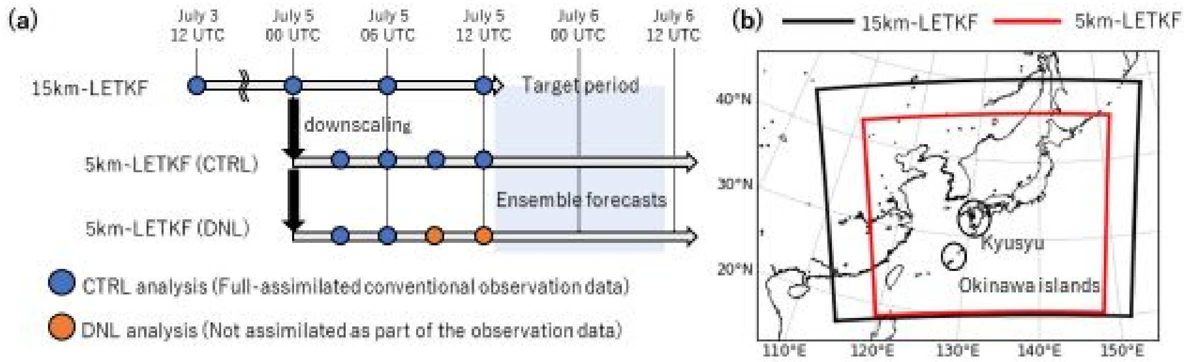

(c)

Experiment	15km-LETKF	5km-LETKF and forecasts
Dimension	273 × 221 × 50 grids	630 × 560 × 50 grids
Resolution	15 km	5 km
Assimilation windows and time slot	6 hours and 1 hour	3 hours and 1 hour
Initial and boundary values	Mesoscale model and the global forecasts	15km-LETKF and the global forecasts
Perturbations	Perturbations in the ensemble predictions from the JMA	15km-LETKF and 5km-LETKF
Ensemble size	51	51
Horizonal localization factor	200 km	100 km

Fig. 2 (a) Experimental time sequence, (b) calculation domain, and (c) setting.

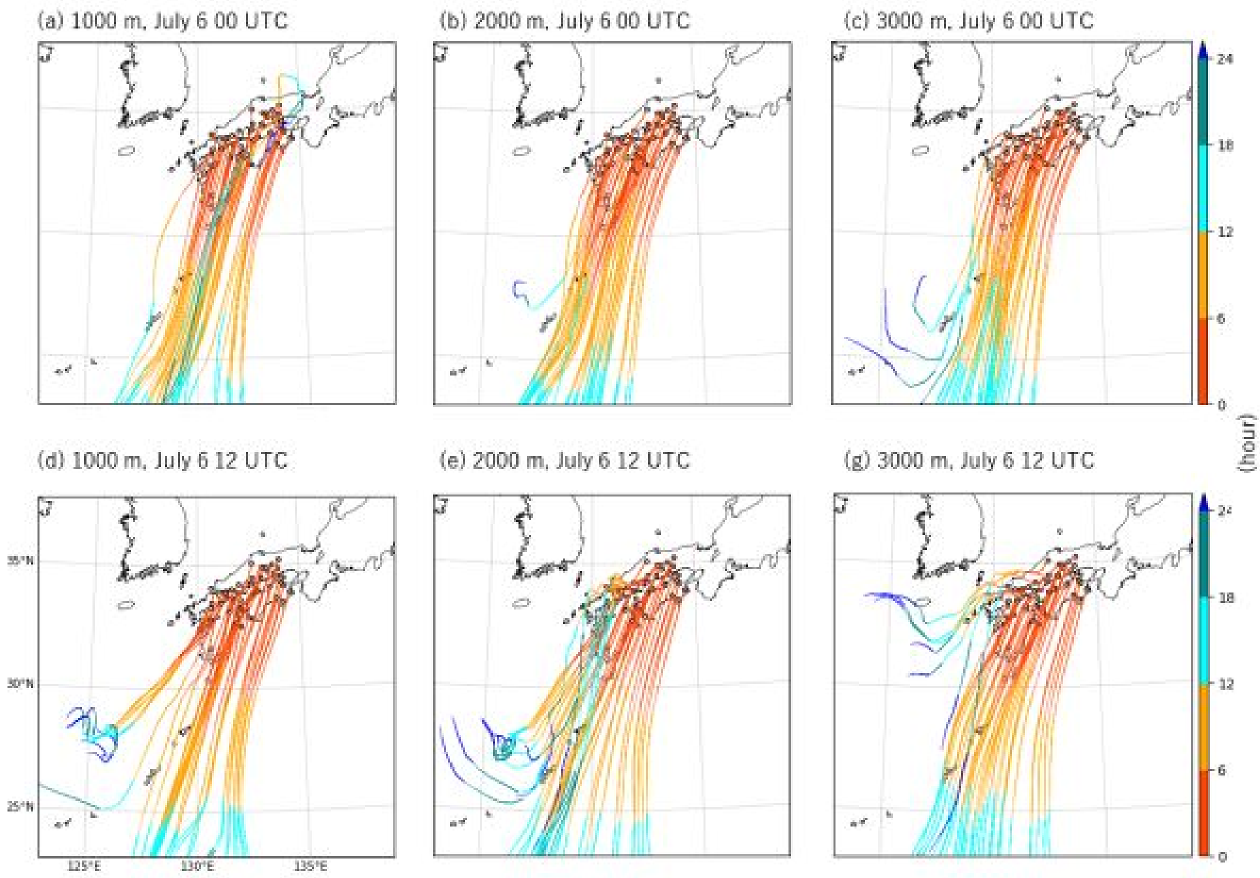

Fig. 3 Backward trajectory analysis over 24 h at heights of 1000 (a and d), 2000 (b and e), and 3000 m (c and g), starting over the rainfall area in western Japan. White circles indicate the initial coordinates, and the colors in each trajectory indicate the elapsed time.

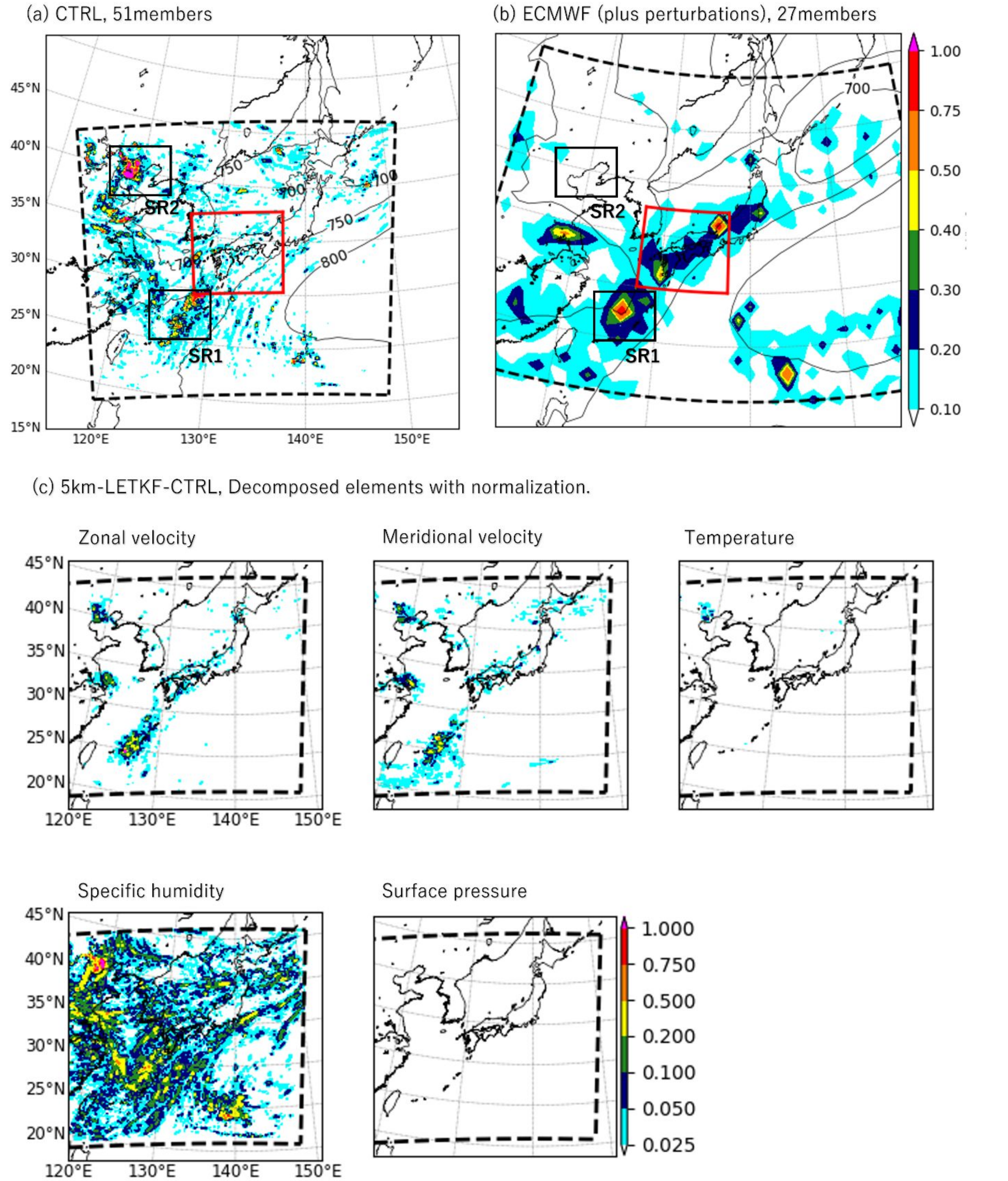

Fig. 4 Ensemble sensitivity of y in Eq. 4 for (a) CTRL and (b) ECMWF at 12 UTC on July 6. Verification area is western Japan (red box). Contours in (a) and (b) denote heights associated with 925-hPa in 50-m intervals. SR1 and SR2 areas (black boxes) are explained

in the text. (c) Components of the 5km-LETKF-CTRL sensitivity: zonal wind (upper left), meridional wind (upper center), temperature (upper right), specific humidity (bottom left), and surface pressure (bottom center).

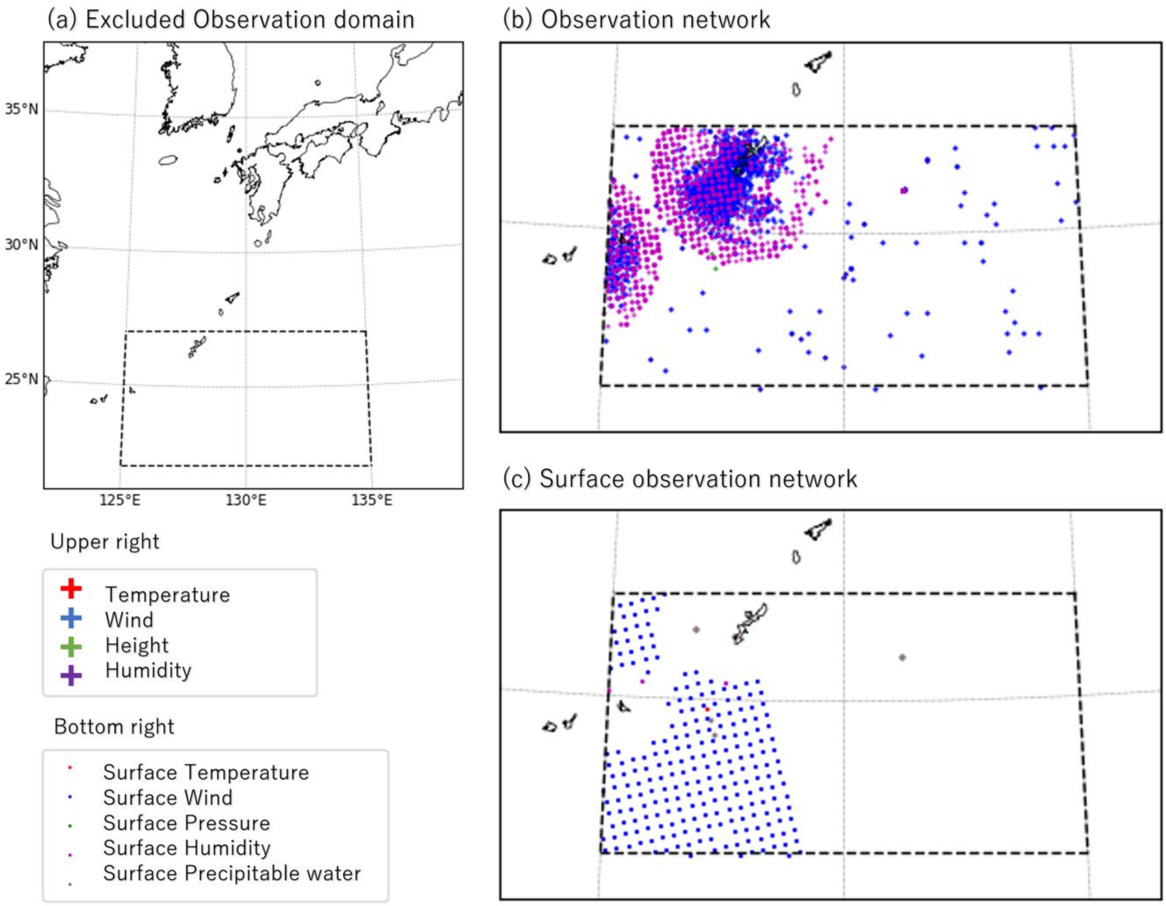

Fig. 5 Distribution of observations excluded from the DNL experiment. The boundary splitting the eastern and western parts of the NOB lies at approximately 130°E. Red, blue, green, purple, and gray indicate the temperature, wind speed, height, specific humidity, and precipitable water, respectively.

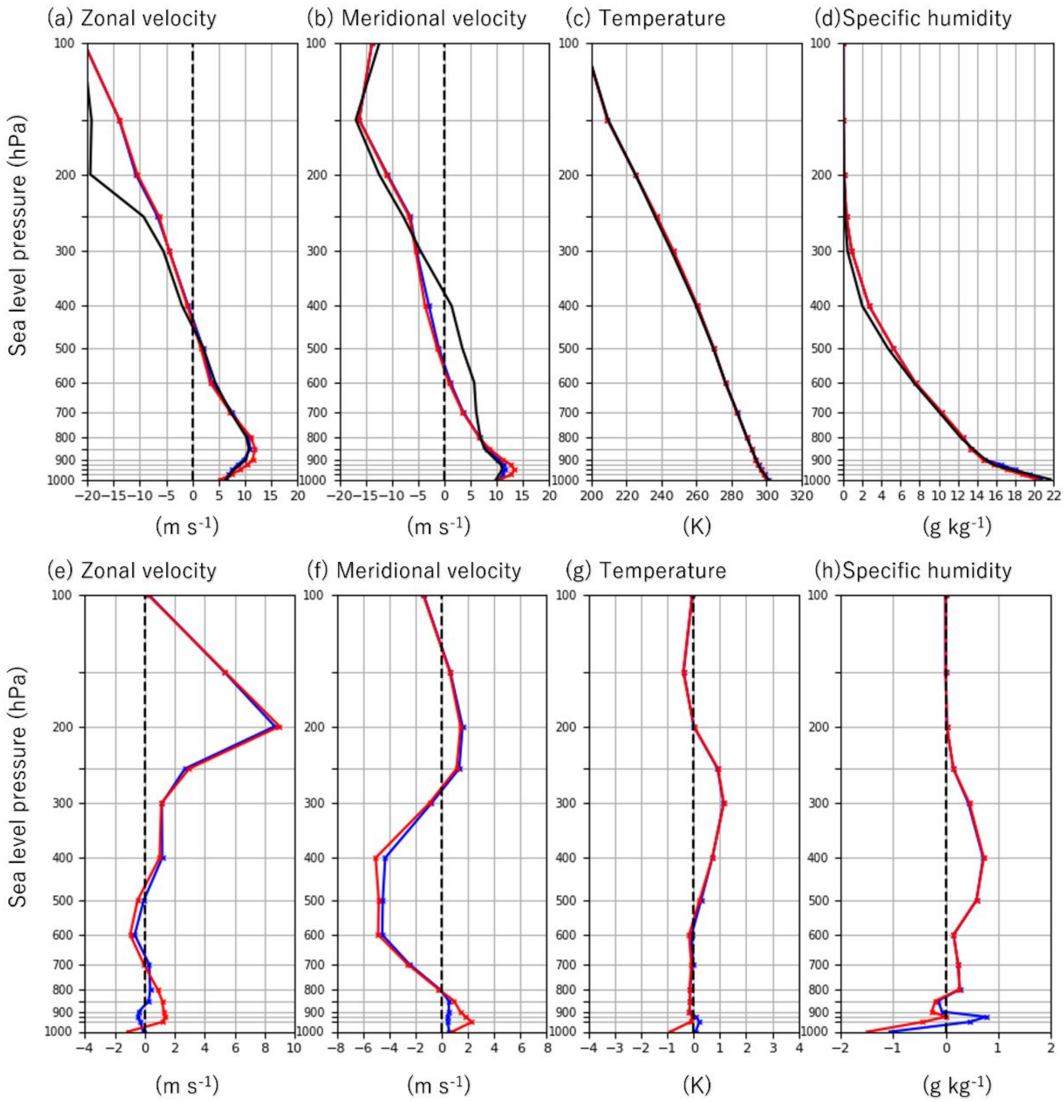

Fig. 6 Vertical profiles obtained using CTRL (blue), DNL (red), JMA meso-analysis (black) (upper), and the difference between the results obtained by CTRL (blue) and DNL (red) minus the meso-analysis (lower) at 12 UTC on July 5, averaged over the western part of the NOB.

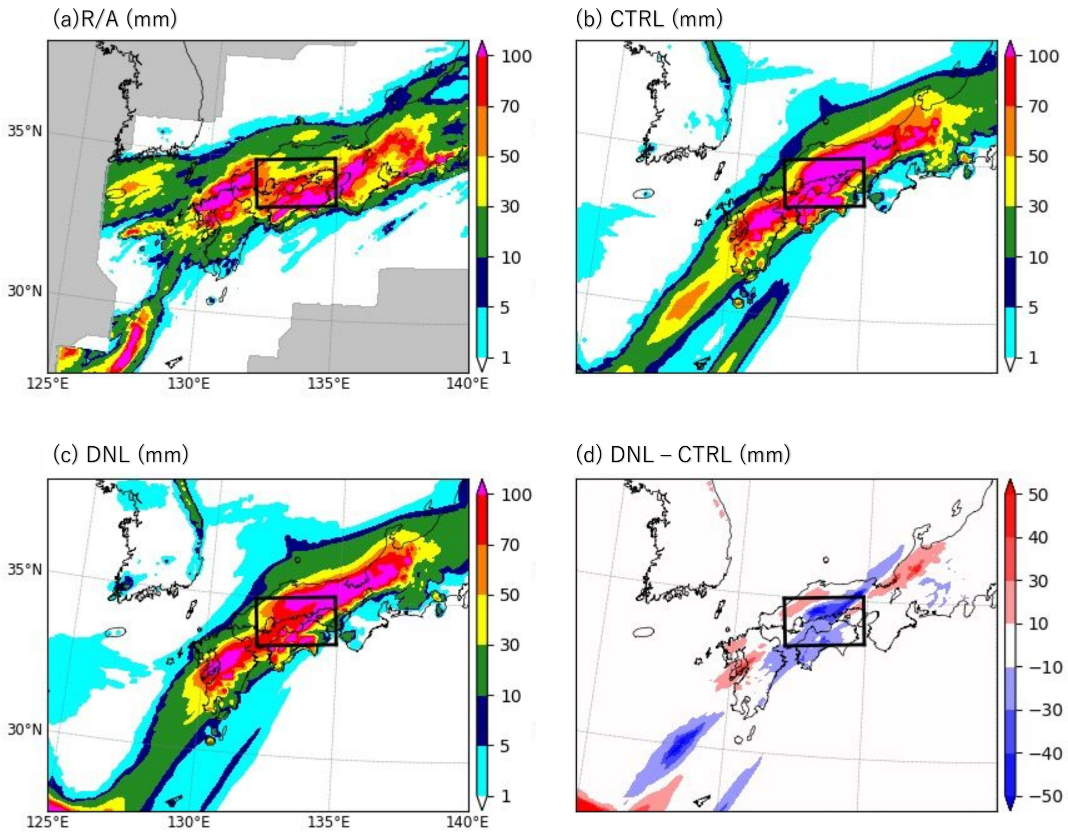

Fig. 7 Accumulated precipitation for 12 h from 00 to 12 UTC on July 6. The (a) R/A, (b) CTRL, (c) DNL predicted rainfall, and (d) DNL minus CTRL. The black box (Setouchi) represents the verification area for the FSS, TS, and BS.

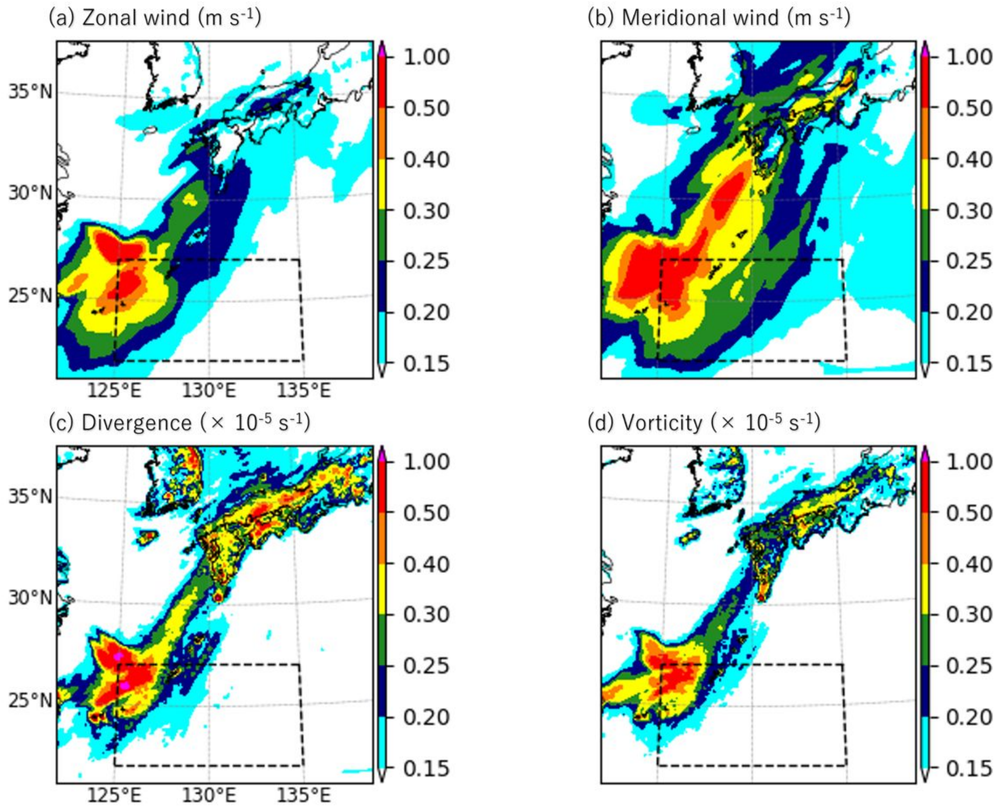

Fig. 8 RMSD of the CTRL and DNL forecasts from 12 UTC on July 5 to 12 UTC on July 6: (a) zonal wind, (b) meridional wind, (c) divergence, and (d) vorticity, normalized to a maximum value of 1. The black dotted box indicates NOB.

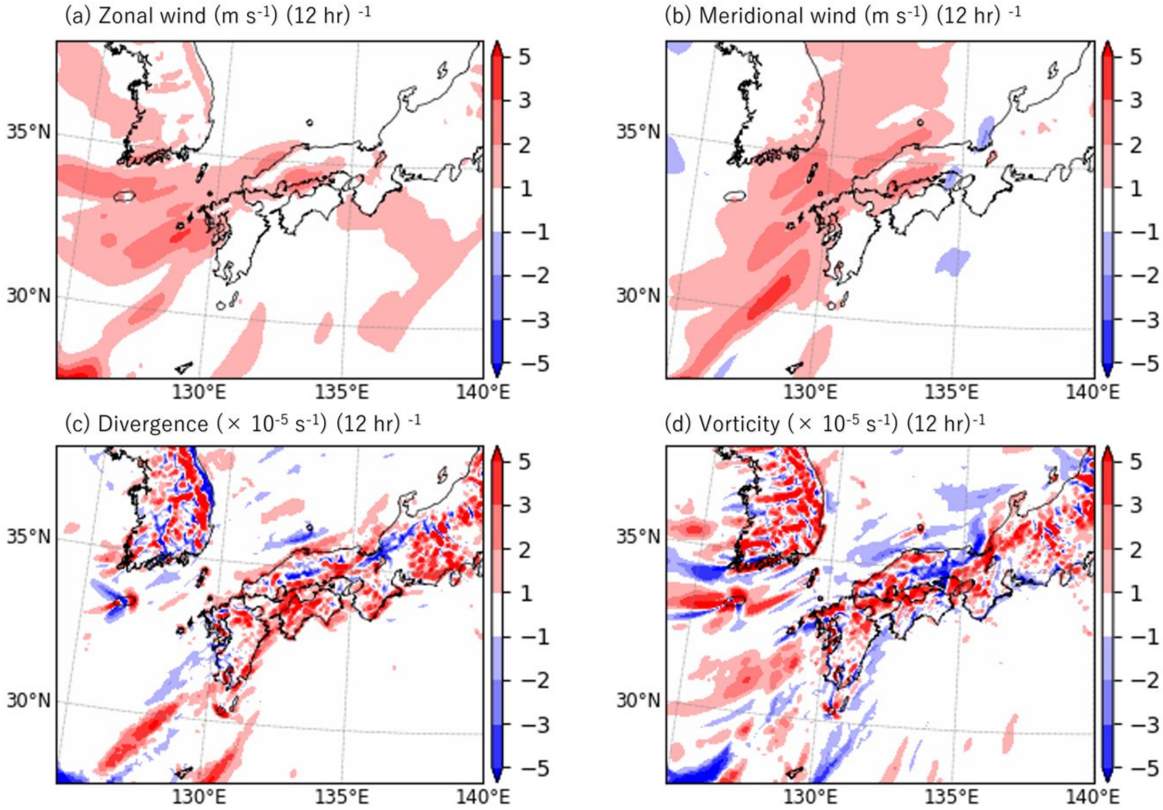

Fig. 9 Differences in the accumulated rainfall over 12 h in the CNTL and DNL (DNL minus CTRL) forecasts, and averaged below 900 hPa from 00 to 12 UTC on July 6: (a) zonal wind, (b) meridional wind, (c) divergence, and (d) vorticity.

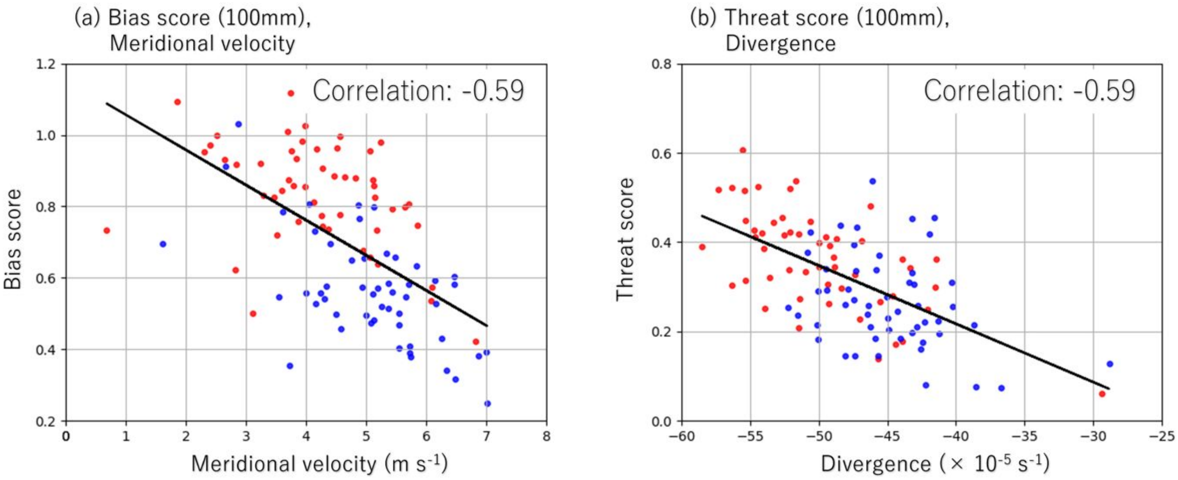

Fig. 10 (a) Scatter plots of the BSs to the 100 mm threshold and the averaged meridional wind below 900 hPa, and (b) the TSs to the 100 mm threshold and the averaged divergence at 900 hPa from 00 to 12 UTC on July 6. The calculation domain is represented by the black box in Fig.7. Red (blue) points illustrate each ensemble member of the CTRL forecast (DNL forecast). The black line represents first-order approximation line.

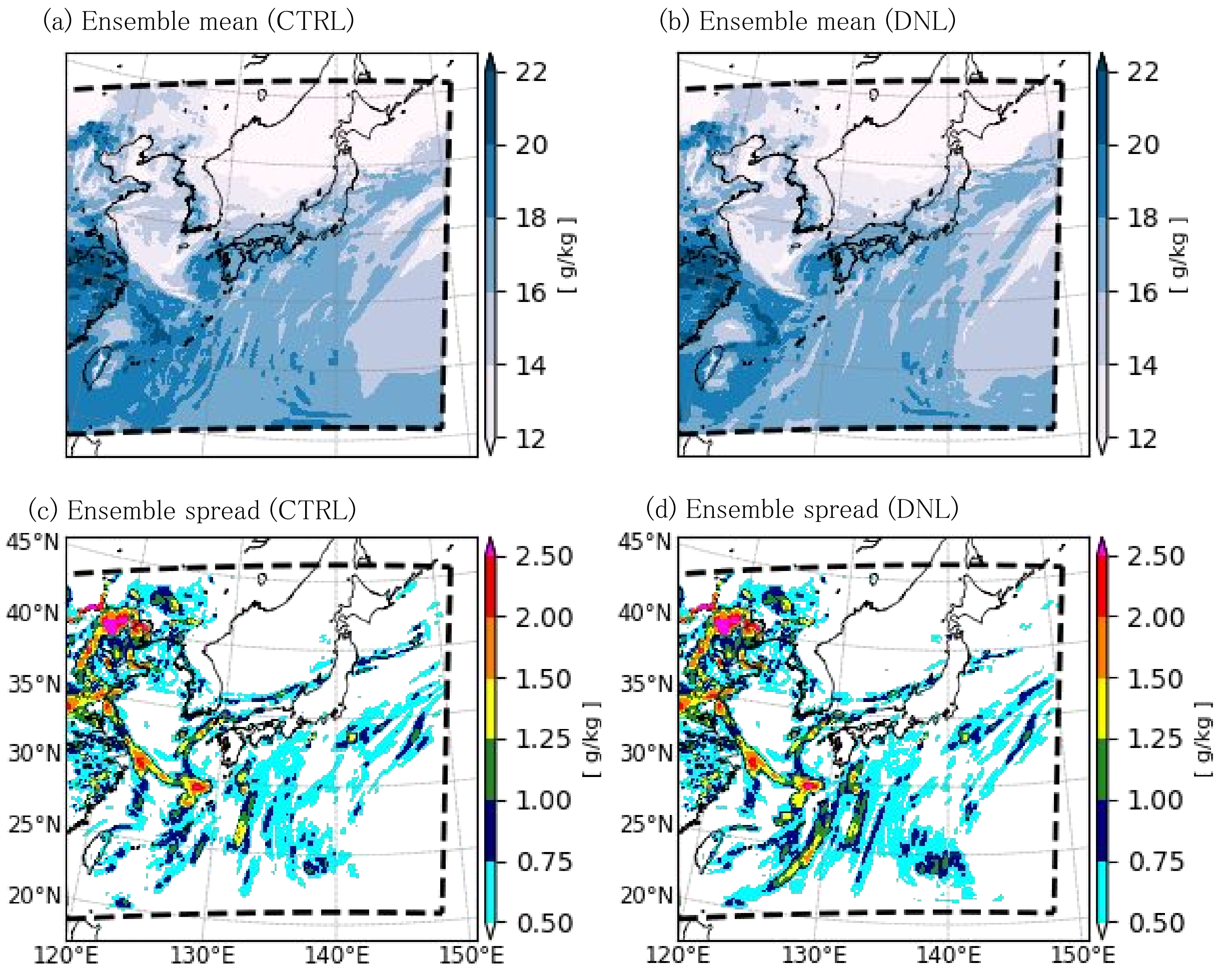

108

109 Fig. 11 Ensemble mean (upper) and spread (lower) of mixing ratio of water vapor at 925
110 hPa, 12 UTC 5 July 2018 (left column: CTRL, right: DNL).

111

List of Tables

Table 1 FSS and BS for 12-h precipitation from 00 to 12 UTC on July 6 over the verification area (black box in Fig. 7).

	Spatial scale (km)	Experiment	Threshold (mm/12 hr)			
			10	50	85	100
FSS	30	CTRL	1.00	0.71	0.53	0.42
		DNL	1.00	0.71	0.37	0.18
	15		0.99	0.66	0.47	0.37
			0.99	0.69	0.35	0.18
	5		0.99	0.61	0.42	0.32
			0.98	0.61	0.29	0.16
BS	5		1.00	0.92	1.02	0.96
			1.00	0.92	0.65	0.47